Published in final edited form as:

Nature. 2013 July 18; 499(7458): 320–323. doi:10.1038/nature12304.

Elucidation of the iron(IV)–oxo intermediate in the non-haem iron halogenase SyrB2

Shaun D. Wong[1,*], **Martin Srnec**[1,*], **Megan L. Matthews**[2,3], **Lei V. Liu**[1], **Yeonju Kwak**[1], **Kiyoung Park**[1], **Caleb B. Bell III**[1], **E. Ercan Alp**[4], **Jiyong Zhao**[4], **Yoshitaka Yoda**[5], **Shinji Kitao**[6], **Makoto Seto**[6], **Carsten Krebs**[2,7], **J. Martin Bollinger Jr.**[2,7], and **Edward I. Solomon**[1]

[1]Department of Chemistry, Stanford University, Stanford, CA 94305

[2]Department of Chemistry, Pennsylvania State University, University Park, PA 16802

[4]Argonne National Laboratory, APS|XFD, 431|D003, Argonne, IL 60439

[5]SPring-8, JASRI, Hyogo 679-5198, Japan

[6]Research Reactor Institute, Kyoto University, Osaka 590-0494, Japan

[7]Department of Biochemistry and Molecular Biology, Pennsylvania State University, University Park, PA 16802

SUMMARY

Mononuclear non-haem iron (NHFe) enzymes catalyse a wide variety of oxidative reactions including halogenation, hydroxylation, ring closure, desaturation, and aromatic ring cleavage. These are highly important for mammalian somatic processes such as phenylalanine metabolism, production of neurotransmitters, hypoxic response, and the biosynthesis of natural products.[1–3] The key reactive intermediate in the catalytic cycles of these enzymes is an $S = 2$ Fe^{IV}=O species, which has been trapped for a number of NHFe enzymes[4–8] including the halogenase SyrB2, the subject of this study. Computational studies to understand the reactivity of the enzymatic NHFe Fe^{IV}=O intermediate[9–13] are limited in applicability due to the paucity of experimental knowledge regarding its geometric and electronic structures, which determine its reactivity. Synchrotron-based nuclear resonance vibrational spectroscopy (NRVS) is a sensitive and effective method that defines the dependence of the vibrational modes of Fe on the nature of the Fe^{IV}=O active site.[14–16] Here we present the first NRVS structural characterisation of the reactive Fe^{IV}=O intermediate of a NHFe enzyme. This Fe^{IV}=O intermediate reacts via an initial H-atom abstraction step, with its subsquent halogenation (native) or hydroxylation (non-native) rebound reactivity being dependent

Correspondence and requests for materials should be addressed to C.K. (ckrebs@psu.edu), J.M.B. (jmb21@psu.edu) or E.I.S. (edward.solomon@stanford.edu).

[3]Current address: Department of Chemical Physiology, The Scripps Research Institute, La Jolla, CA 92307

[*]S.D.W. and M.S. are co-first authors.

Supplementary Information is available in the online version of the paper.

Author Contributions S.D.W. and M.S. contributed equally to this work. E.I.S., C.K. and J.M.B. designed the experiments. S.D.W., M.S., M.L.M., L.V.L., Y.K., K.P. and C.B.B. performed the experiments. S.D.W., M.S. and E.I.S. analysed the data and wrote the manuscript. E.E., J.Z., Y.Y., S.K. and M.Seto provided technical assistance at the sychrotron beamlines.

The authors declare no competing financial interests.

on the substrate.[17] A correlation of the experimental NRVS data to electronic structure calculations indicates that the substrate is able to direct the orientation of the Fe^{IV}=O intermediate, presenting specific frontier molecular orbitals (FMOs) which can activate the selective halogenation versus hydroxylation reactivity.

SyrB2, an α-ketoglutarate (αKG)-dependent NHFe enzyme found in *Pseudomonas syringae* pv. *Syringae*, halogenates the methyl group of L-Thr using nonribosomal peptide synthetase machinery.[18] The Fe^{II} active site is ligated by 2 His and 1 halide (Cl^-/Br^-) (see Supplementary Fig. 1), in contrast to the 2-His/1-carboxylate 'facial triad' of other NHFe enzymes.[1,2,4,5,8] While their mechanisms of O_2 activation leading to the highly-reactive *S* = 2 Fe^{IV}=O intermediate are thought to be similar, there is a notable divergence in their subsequent catalytic cycles (Fig. 1). The Fe^{IV}=O species abstracts an H-atom from the substrate to form an Fe^{III}—OH species and a substrate radical; in hydroxylases, the subsequent step is $HO^{\bullet}$ rebound to form a hydroxylated product,[1,2] but in SyrB2 the native L-Thr substrate is chlorinated instead, and the 4-Cl-L-Thr product is utilised in the biosynthesis of the phytotoxin syringomycin E.[18] Owing to their reactivity, Fe^{IV}=O intermediates in enzymes are challenging to trap and characterise. For SyrB2, however, use of the non-native substrate L-cyclopropylglycine (L-Cpg) and the heterologous substrate carrier protein CytC2 has provided a long-lived species at the concentrations required for spectroscopic investigation.[17,19]

Nuclear resonance vibrational spectroscopy (NRVS) utilises 3rd-generation-synchrotron radiation to probe the vibrational sidebands of the ^{57}Fe Mössbauer nuclear-resonant peak at 14.4 keV.[20–22] NRVS is a site-selective technique allowing the observation of only normal modes involving Fe motion, which makes it ideal for studying iron-dependent enzymes without interference from protein backbone modes. (SyrB2)Fe^{IV}=O can be generated in high purity with both Cl^- and Br^- ligation of the Fe^{IV}=O unit, providing a mass perturbation that aids in the assignment of NRVS peaks and ultimately the structure of the intermediate. The NRVS methodology is coupled with spectroscopically-calibrated density functional theory (DFT) calculations to evaluate specific FMOs responsible for H-atom abstraction that can selectively lead to halogenation or hydroxylation depending on the substrate.

The NRVS partial vibrational density-of-states (PVDOS) spectra of L-Cpg–*S*–CytC2-bound [(SyrB2)Cl—Fe^{IV}=O] (**SyrB2–Cl**) and [(SyrB2)Br—Fe^{IV}=O] (**SyrB2–Br**) are shown in Fig. 2. For practical considerations (see Methods), data collection was restricted to < 600 cm^{-1}; modes in this region are affected by large (Cl/Br, *vide infra*) but not small (^{16}O/^{18}O, see Supplementary Fig. 2) mass perturbations. There are three distinct features for each species as indicated by the bracketed energy regions: 1 (340–400 cm^{-1}), 2 (285–340 cm^{-1}) and 3 (200–285 cm^{-1}). For the higher-energy regions 1 and 2, the peaks of **SyrB2–Cl** are more intense. However, for the low-energy region 3, the peak envelope for **SyrB2–Br** is considerably more intense and shifted to lower energy.

Previous computational studies on the Cl—Fe^{IV}=O intermediate of SyrB2 predicted 6-coordinate (6C) structures with the succinate bound as a bidentate ligand to Fe.[9–12] The DFT-calculated NRVS spectra of these 6C structures (Supplementary Fig. 3) do not

reproduce the splitting pattern and intensity distribution of the experimental data, and can thus be eliminated from consideration.

In order to generate and evaluate suitable structural candidates, the O_2 reaction coordinate taking SyrB2 to its Fe^{IV}=O intermediate (Fig. 1) was pursued using DFT calculations. The initial structure was taken from the crystal structure of the SyrB2 Fe^{II} active site with the αKG cofactor and Cl^- bound (Supplementary Fig. 3)[23] and the native substrate L-Thr positioned according to a molecular docking procedure;[12] its side-chain was also modified into the non-native substrate L-Cpg to generate a second starting structure. Application of the spectroscopically-calibrated DFT methodology used for a related αKG-dependent mononuclear NHFe enzyme[24] resulted in an equivalent O_2 reaction coordinate for the Fe^{II} active site of SyrB2 (Supplementary Figs. 4 and 5a,b).

This O_2 reaction coordinate leads to $\mathbf{1_{Cpg}–Cl}$ (Fig. 3b) and $\mathbf{1_{Thr}–Cl}$ (Supplementary Fig. 5b) with L-Cpg and L-Thr respectively; both are 5-coordinate (5C) trigonal bipyramidal (TBP) Fe^{IV}=O structures possessing an axial oxo group and a monodentate succinate. Significantly, in both cases, the Fe—oxo vector is oriented perpendicularly to the target substrate C–H bond, raising interesting implications about π-channel reactivity.[25,26]

$\mathbf{1_{Cpg}–Cl}$ was evaluated as a structural candidate for the Fe^{IV}=O intermediate in the NRVS sample. The geometry-optimised Fe—oxo and Fe—Cl bond lengths (Fig. 3b) of $\mathbf{1_{Cpg}–Cl}$ are in close agreement with the experimental extended X-ray absorption fine structure (EXAFS) values (1.66 Å and 2.31 Å respectively).[7] The Br^- cognate $\mathbf{1_{Cpg}–Br}$ was generated by replacing Cl^- with Br^- and reoptimising the structure; its Fe—Br bond length of 2.45 Å (Fig. 3b) agrees well with the EXAFS value of 2.43 Å for the related halogenase CytC3.[6] Thus, these 5C TBP intermediates $\mathbf{1_{Cpg}–X}$ (**X = Cl/Br**) resulting from the O_2 reaction coordinate were used for comparison with the experimental NRVS data on the SyrB2 Fe^{IV}=O intermediates **SyrB2–X**.

As seen in Fig. 3, the 5C TBP species $\mathbf{1_{Cpg}–X}$ result in DFT-predicted spectra that reproduce the experimental spectra. First, there are three distinct peaks falling within the energy regions of 200–275 cm^{-1}, 275–340 cm^{-1} and 340–400 cm^{-1}, matching regions 3, 2, and 1 in Fig. 2. Second, the intensities of the peaks in the two higher-energy regions are greater for $\mathbf{1_{Cpg}–Cl}$ than for $\mathbf{1_{Cpg}–Br}$, while the intensity of the peak envelope in the lowest-energy region for $\mathbf{1_{Cpg}–Br}$ is greater and shifted to lower energy with respect to that of $\mathbf{1_{Cpg}–Cl}$, reproducing the spectral intensity distributions of the experimental data (Fig. 2). Other 5C and 6C structures were generated as possible candidates for the Fe^{IV}=O species, starting from $\mathbf{1_{Cpg}–X}$ and shifting either the Fe-ligating atoms or the hydrogen-bonding network to the oxo group (Supplementary Fig. 6). From the predicted NRVS spectra of these structures and of the structures generated in previous (computational) studies (Supplementary Fig. 3), all structures except 5C TBP can be eliminated due to their poor agreement with the experimental NRVS data.

Correlating the DFT-calculated spectra of 5C TBP $\mathbf{1_{Cpg}–X}$ (Fig. 3) with the experimental spectra (Fig. 2), the NRVS peaks can be assigned to four normal modes (Fig. 4): (i) the feature in region 1 (Fig. 2) originates from the Fe—succinate stretch; (ii) the feature in

region 2 is composed of a pair of *trans*-axial bend modes (these would be degenerate in strict TBP symmetry, but are calculated to split in energy because of the wider equatorial X—Fe—succinate angle of 143°);[14] the lowest-energy region 3 has a peak envelope calculated to contain (iii) the *trans*-axial stretch and (iv) the Fe—X stretch, with the Fe—Br stretch being lower in energy by 30 cm^{-1} and more intense by 1.5 times. The redistribution in intensity is attributed to the mass perturbation of the Br, which has almost no motion in the Fe—X stretching mode and consequently induces greater Fe motion in the mode. This Fe motion is borrowed from higher-energy modes, as analysed in Supplementary Fig. 7. The NRVS peak pattern of **SyrB2–X** parallels that of a crystallographically-characterised TBP *S* = 2 Fe^{IV}=O model complex (Supplementary Fig. 8),[15] further demonstrating the sensitivity of NRVS to geometric structure.

Note that two distinct Fe^{IV} species are detected by Mössbauer, differing in quadrupole splitting, ΔE_Q (see Supplementary Fig. 9) in each Fe^{IV}=O intermediate generated.[7] A possible explanation for this speciation lies in the hydrogen-bonding interactions with the oxo group: $\mathbf{1_{Cpg}–Cl}$ has two (with Arg_{254} and H_2O), while $\mathbf{1_{Thr}–Cl}$ has one (with H_2O). Their predicted NRVS spectra are similar (Supplementary Figs. 6 and 10a), but their calculated ΔE_Q's are different, with that of $\mathbf{1_{Cpg}–Cl}$ (−0.50 mm s^{-1}) being smaller in magnitude than that of $\mathbf{1_{Thr}–Cl}$ (−0.71 mm s^{-1}). Decreasing the number of hydrogen bonds strengthens the Fe—oxo bond, thus increasing the magnitude of (negative) ΔE_Q (Supplementary Fig. 10a and Supplementary Table 1). These calculations suggest that variability in hydrogen-bonding interactions with the oxo group results in Fe^{IV} speciation, not some structural difference.

For the native L-Thr substrate, starting from the O_2-reaction-coordinate-derived Fe^{IV}=O species $\mathbf{1_{Thr}–Cl}$, having its Fe—oxo vector perpendicular to C–H (Supplementary Figure 5b), the H-atom abstraction reactivity was computationally evaluated (Fig. 5). The target C–H approaches in a π-trajectory, transferring an α-electron into the oxo π-FMO, resulting in an $Fe^{III}_{(S=5/2)}$—OH first product ($\mathbf{1_{Thr}–Fe^{III}OH}$). The free-energy barrier $\Delta G^{‡}$ for this π-pathway is +100.4 kJ mol^{-1}, in reasonable agreement with the experimental value of +79.4 kJ mol^{-1}.[7] A number of possible explanations have been considered for the subsequent $Cl^{•}$ rebound;[17,27] here we show that in this first product, the substrate radical is positioned closer to the Cl than to the OH ligand of Fe^{III} (consideration of their ionic radii places Cl 0.5 Å closer than OH), and OH is also stabilised by hydrogen-bonding to succinate (Fig. 5, *right*). This conformation disfavours $HO^{•}$ rebound but is well-oriented for $Cl^{•}$ rebound, as observed experimentally with this native substrate. This perpendicular Fe—oxo orientation is, for the 6C structures proposed in previous computational studies,[9–12] inaccessible via the O_2-activation pathway because a bidentate succinate would block the oxo group from reorienting.

Evaluation of the reaction coordinate for O—O cleavage leading to the Fe^{IV}=O species (Supplementary Fig. 5) revealed that the positioning of L-Thr is fixed by two hydrogen-bonding interactions (–OH and $–NH_3^+$) to Glu_{102}. This configuration results in the perpendicular orientation of the Fe^{IV}—oxo vector relative to the substrate C–H bond. However, the alternative substrate L-Nva lacks the –OH group, and thus its $–NH_3^+$ group can rotate to form a hydrogen bond with the O—O (peroxy) bridge, leading to a structure with

an Fe—oxo vector oriented towards the substrate C–H bond (Supplementary Fig. 5c). An analogous L-Thr orientation was thus generated in order to evaluate its H-atom abstraction trajectory while maintaining the same C–H bond (Fig. 5, *left*).

For this orientation, the C–H approaches the Fe—oxo unit in a σ-trajectory, transferring an α-electron into the oxo σ-FMO to give an $Fe^{III}_{(S=5/2)}$—OH product; this σ-pathway has a $\Delta G^{\ddagger}$ of +70.2 kJ mol^{-1} (Fig. 5). Relative to the π-pathway Fe^{III}—OH product, this Fe^{III}—OH has the substrate radical closer to the OH ligand than the Cl (by 0.5 Å, based on ionic radii), and OH has no hydrogen-bonding partner. The parallel Fe—oxo orientation therefore favours $HO^{\bullet}$ rebound, as is observed experimentally for the non-native substrate L-Nva.[17] We also note that the barrier for π-attack is somewhat higher than that for σ-attack, which is consistent with the higher barrier observed experimentally for halogenation relative to hydroxylation (by ~17 kJ mol^{-1}),[17] reflecting halogenation selectivity over efficiency.

In summary, we have performed the first NRVS structural characterisation of a NHFe enzyme oxygen intermediate and defined it to be a 5C TBP site with an axial Fe^{IV}=O bond. The *native-substrate-bound* O_2 reaction coordinate reproduces this 5C TBP structure and gives an intermediate with its Fe—oxo vector perpendicular to the substrate C–H bond; this Fe—oxo orientation is active in H-atom abstraction, via its π*-FMO. This positions the substrate radical favourably for $Cl^{\bullet}$ rebound, thus defining a selective mechanism in halogenases for chlorination of the native substrate. Alternatively, with a *non-native substrate*, variation in the O_2 reaction coordinate can lead to an intermediate with its Fe—oxo vector parallel to the substrate C–H bond, leading to H-atom abstraction via a σ-pathway and a substrate radical positioned for $HO^{\bullet}$ rebound and resultant hydroxylation.

METHODS (ONLINE)

Computational Methods

Spin-unrestricted DFT calculations were performed using the Turbomole 6.3[30] and Gaussian 09[31] programs. Turbomole 6.3 was used to perform geometry optimisations and frequency calculations of the structural candidates in Supplementary Fig. 6, with the BP86[32–34] exchange-correlation functional and the double-ζ def2-SVP basis set.[35] Single-point energies were recomputed using the larger triple-ζ basis set def2-TZVP.[35] Turbomole calculations were expedited by expanding the Coulomb integrals in an auxiliary basis set, using the *RI*-J approximation.[36,37] Solvation effects were taken into account by using the Conductor-like Screening Model (COSMO) method[38,39] with a dielectric constant $\varepsilon_r = 4$ as is appropriate for the protein environment (the COSMO radii were set up to: (H) 1.30 Å, (C) 2.00 Å, (N) 1.83 Å, (O) 1.72 Å, (Cl) 2.05 Å, (Br) 2.16 Å, (S) 2.16 Å and (Fe) 2.23 Å). This is referred to as the *RI*-BP86/def2-SVP(or def2-TZVP)/COSMO approach or level of theory.

Gaussian 09 was used to perform geometry optimisations and frequency calculations of the structural candidates $\mathbf{1_{Cpg}–X}$ in Fig. 3, with the functional/basis set combination BP86/6-311G*.[40–43] Solvation effects were taken into account with the Polarized Continuum Model (PCM),[44–47] using $\varepsilon = 4.0$. This is referred to as the BP86/6-311G*/PCM approach or level of theory.

NRVS PVDOS spectra were simulated by fitting the DFT-calculated mode composition factor[48]

$$e^2_{n,Fe} = \frac{m_{Fe} r^2_{n,Fe}}{\sum_{i}^{atoms} m_i r^2_{n,i}}$$

for each normal mode *n* with individual Gaussians of FWHM 15 cm^{-1}, using the *gennrvs* script.[49]

Mössbauer isomer shifts and quadrupole spittings were calculated according to published methods.[50]

The initial structure of the SyrB2 Fe^{II} active site used for DFT calculations was taken from its crystal structure (Supplementary Fig. 1 and ref. 23). Inclusion of the substrate (L-Cpg-SH, where the terminal –SH group represents truncation at the thioester linkage to the phosphopantetheine cofactor) was modeled according to ref. 12. Except where stated, the S atom of the substrate was frozen during geometry optimisation. Note that the substrate does indeed fit well in the cavity of the active site (Supplementary Fig. 1d).

The O_2-reaction coordinate starting from the SyrB2–Cl Fe^{II} active site was pursued analogously to ref. 24, at the *RI*-BP86/def2-SVP(def2-TZVP)/COSMO level of theory. The complete O_2-reaction coordinate for the L-Cpg-bound active site (with either Cl^- or Br^-) is shown in Supplementary Fig. 4, and Supplementary Fig. 5 shows the final O—O cleavage step, leading to the Fe^{IV}=O intermediate, for three versions of the active site containing L-Cpg (inert substrate), L-Thr (native substrate), and L-Nva (non-native substrate).

The H-atom abstraction reaction coordinates of the SyrB2–Cl Fe^{IV}=O intermediate were evaluated using the Turbomole 6.3 program.[30] $\mathbf{1_{Thr}–Cl}$ was optimised at the B3LYP[51–53]+D2/def2-SVP level (where +D2 stands for the second version of Grimme's empirical dispersion correction[54,55]). Thermodynamic corrections to give enthalpic (ΔH) and Gibbs (ΔG) energies were calculated at T = 278.15 K to reproduce experimental conditions.[7] Single-point energies were calculated at the B3LYP+D2/def2-TZVP/COSMO(ε_r=4.0) level. The calculated NRVS spectra of these Thr-bound species (Supplementary Fig. 10) are similar to those of their Cpg-bound counterparts (Supplementary Fig. 6), showing that the substrate does not affect the NRVS spectra because it is not directly coordinated to the Fe centre. Starting with $\mathbf{1_{Thr}–Cl}$ and $\mathbf{2_{Thr}–Cl}$ as the reactant complexes (RCs), each H-atom abstraction reaction was pursued along the oxo---H(L-Thr) coordinate and each transition state (TS) was optimised from the highest-energy structure along the reaction coordinate. An internal reaction coordinate was calculated from each optimised TS (forward) to obtain the product (Fe^{III}—OH + substrate radical) and (backward) to confirm the validity of the RC structure.

Supplementary Material

Refer to Web version on PubMed Central for supplementary material.

Acknowledgements

Funding for research was provided by the National Institutes of Health (GM-40392 to E.I.S. and GM-69657 to J.M.B. and C.K.) and the National Science Foundation (MCB-0919027 to E.I.S. and MCB-642058 and CHE-724084 to J.M.B. and C.K.). Work at the Advanced Photon Source is supported by the Department of Energy, Office of Science, Contract DE-AC-02-06CH11357. Synchrotron experiments at SPring-8 were performed with the approval of the Japan Synchrotron Radiation Research Institute (JASRI) (Proposal No. 2010B1569). M.S. thanks the RullÌšek group at the IOCB, Prague, for use of their computational resources.

REFERENCES

1. Solomon EI, et al. Geometric and electronic structure/function correlations in non-heme iron enzymes. Chem. Rev. 2000; 100:235–350. [PubMed: 11749238]
2. Costas M, Mehn MP, Jensen MP, Que L Jr. dioxygen activation at mononuclear nonheme iron active sites: enzymes, models, and intermediates. Chem. Rev. 2004; 104:939–986. [PubMed: 14871146]
3. Vaillancourt FH, Yeh E, Vosburg DA, Garneau-Tsodikova S, Walsh CT. Nature#x00027;s inventory of halogenation catalysts: oxidative strategies predominate. Chem. Rev. 2006; 106:3364–3378. [PubMed: 16895332]
4. Krebs C, Galoni#x00107; Fujimori D, Walsh CT, Bollinger JM Jr. Non-heme Fe(IV)-oxo intermediates. Acc. Chem. Res. 2007; 40:484–492. [PubMed: 17542550]
5. Eser BE, et al. Direct spectroscopic evidence for a high-spin Fe(IV) intermediate in tyrosine hydroxylase. J. Am Chem. Soc. 2007; 129:11334–11335. [PubMed: 17715926]
6. Galoni#x00107; Fujimori D, et al. Spectroscopic evidence for a high-spin Br-Fe(IV)-oxo intermediate in the alpha-ketoglutarate-dependent halogenase CytC3 from *Streptomyces*. J. Am Chem. Soc. 2007; 129:13408–13409. [PubMed: 17939667]
7. Matthews ML, et al. Substrate-triggered formation and remarkable stability of the C–H bond-cleaving chloroferryl intermediate in the aliphatic halogenase, SyrB2. Biochemistry. 2009; 48:4331–4343. [PubMed: 19245217]
8. Panay AJ, Lee M, Krebs C, Bollinger JM Jr, Fitzpatrick PF. Evidence for a high-spin Fe(IV) species in the catalytic cycle of a bacterial phenylalanine hydroxylase. Biochemistry. 2011; 50:1928–1933. [PubMed: 21261288]
9. Pandian S, Vincent MA, Hillier IH, Burton NA. Why does the enzyme SyrB2 chlorinate, but does not hydroxylate, saturated hydrocarbons? A density functional theory (DFT) study. Dalton Trans. 2009:6201–6207. [PubMed: 20449117]
10. Kulik HJ, Blasiak LC, Marzari N, Drennan CL. First-principles study of non-heme Fe(II) halogenase SyrB2 reactivity. J. Am Chem. Soc. 2009; 131:14426–14433. [PubMed: 19807187]
11. de Visser SP, Latifi R. Carbon dioxide: a waste product in the catalytic cycle of alpha-ketoglutarate dependent halogenases prevents the formation of hydroxylated by-products. J. Phys. Chem. B. 2009; 113:12–14. [PubMed: 19061416]
12. Borowski T, Noack H, Radoń M, Zych K, Siegbahn PEM. Mechanism of selective halogenation by SyrB2: a computational study. J. Am Chem. Soc. 2010; 132:12887–12898. [PubMed: 20738087]
13. Usharani D, Janardanan D, Shaik S. Does the TauD enzyme always hydroxylate alkanes, while an analogous synthetic non-heme reagent always desaturates them? J. Am Chem. Soc. 2012; 133:176–179. [PubMed: 21171573]
14. Bell CB, et al. A combined NRVS and DFT study of Fe^{IV}=O model complexes: a diagnostic method for the elucidation of non-heme iron enzyme intermediates. Angew. Chem. Intl. Ed. 2008; 47:9071–9074.
15. Wong SD, et al. Nuclear resonance vibrational spectroscopy on the Fe^{IV}=O S = 2 non-heme site in TMG_3tren: experimentally calibrated insights into reactivity. Angew. Chem. Intl. Ed. 2011; 50:3215–3218.
16. Park K, et al. Nuclear resonance vibrational spectroscopic and computational study of high-valent diiron complexes relevant to enzyme intermediates. Proc. Natl Acad. Sci. USA. 2013; 110:6275–6280. [PubMed: 23576760]

17. Matthews ML, et al. Substrate positioning controls the partition between halogenation and hydroxylation in the aliphatic halogenase, SyrB2. Proc. Natl Acad. Sci. USA. 2009; 106:17723–17728. [PubMed: 19815524]
18. Vaillancourt FH, Yin J, Walsh CT. SyrB2 in syringomycin E biosynthesis is a nonheme Fe^{II} α-ketoglutarate- and O_2-dependent halogenase. Proc. Natl Acad. Sci. USA. 2005; 102:10111–10116. [PubMed: 16002467]
19. Krebs C, et al. Novel approaches for the accumulation of oxygenated intermediates to multi-millimolar concentrations. Coord. Chem. Rev. 2013; 257:234–243.
20. Seto M, Yoda Y, Kikuta S, Zhang X, Ando M. Observation of nuclear resonant scattering accompanied by phonon excitation using synchrotron radiation. Phys. Rev. Lett. 1995; 74:3828–3831. [PubMed: 10058307]
21. Chumakov AI, Sturhahn W. Experimental aspects of inelastic nuclear resonance scattering. Hyperfine Interact. 1999; 123–124:781–808.
22. Sage JT, et al. Nuclear resonance vibrational spectroscopy of a protein active-site mimic. J. Phys.: Condens. Matter. 2001; 13:7707–7722.
23. Blasiak LC, Vaillancourt FH, Walsh CT, Drennan CL. Crystal structure of the non-haem iron halogenase SyrB2 in syringomycin biosynthesis. Nature. 2006; 440:368–371. [PubMed: 16541079]
24. Diebold AR, et al. Activation of α-keto acid-dependent dioxygenases: application of an $\{FeNO\}^7$/$\{FeO_2\}^8$ methodology for characterizing the initial steps of O_2 activation. J. Am Chem. Soc. 2011; 133:18148–18160. [PubMed: 21981763]
25. Neidig ML, et al. Spectroscopic and electronic structure studies of aromatic electrophilic attack and hydrogen-atom abstraction by non-heme iron enzymes. Proc. Natl Acad. Sci. USA. 2006; 103:12966–12973. [PubMed: 16920789]
26. Srnec M, Wong SD, England J, Que L, Solomon EI. π-frontier molecular orbitals in $S = 2$ ferryl species and elucidation of their contributions to reactivity. Proc. Natl Acad. Sci. USA. 2012; 109:14326–14331. [PubMed: 22908238]
27. Comba P, Wunderlich S. Iron-catalyzed halogenation of alkanes: modeling of nonheme halogenases by experiment and DFT calculations. Chem. Eur. J. 2010; 16:7293–7299. [PubMed: 20458709]
28. Alp EE, Mooney TM, Toellner T, Sturhahn W. Nuclear resonant scattering beamline at the Advanced Photon Source. Hyperfine Interact. 1994; 90:323–334.
29. Yoda Y, et al. Nuclear resonant scattering beamline at SPring-8. Nucl. Instrum. Methods A. 2001; 467–468:715–718.

[REFERENCES FOR ONLINE METHODS SECTION]

30. Ahlrichs R, Bär M, Häser M, Horn H, Kölmel C. Electronic structure calculations on workstation computers: the program system Turbomole. Chem. Phys. Lett. 1989; 162:165–169.
31. Frisch, MJ., et al. Gaussian 09, Revision A.1. Wallingford CT: Gaussian, Inc.; 2009.
32. Becke AD. Density-functional exchange-energy approximation with correct asymptotic behavior. Phys. Rev. A. 1988; 38:3098–3100. [PubMed: 9900728]
33. Perdew J. Density-functional approximation for the correlation energy of the inhomogeneous electron gas. Phys. Rev. B. 1986; 33:8822–8824.
34. Vosko SH, Wilk L, Nusair M. Accurate spin-dependent electron liquid correlation energies for local spin density calculations: a critical analysis. Can. J. Phys. 2012; 58:1200–1211.
35. Weigend F, Ahlrichs R. Balanced basis sets of split valence, triple zeta valence and quadruple zeta valence quality for H to Rn: design and assessment of accuracy. Phys. Chem. Chem. Phys. 2005; 7:3297–3305. [PubMed: 16240044]
36. Eichkorn K, Treutler O, Öhm H, Häser M, Ahlrichs R. Auxiliary basis sets to approximate Coulomb potentials. Chem. Phys. Lett. 1995; 240:283–290.
37. Eichkorn K, Weigend F, Treutler O, Ahlrichs R. Auxiliary basis sets for main row atoms and transition metals and their use to approximate Coulomb potentials. Theoret. Chim. Acta. 1997; 97:119–124.

38. Klamt A, Schüürmann G. COSMO: a new approach to dielectric screening in solvents with explicit expressions for the screening energy and its gradient. J. Chem. Soc., Perkin Trans. 1993; 20:799–805.
39. Schäfer A, Klamt A, Sattel D, Lohrenz JCW, Eckert F. COSMO implementation in Turbomole: extension of an efficient quantum chemical code towards liquid systems. Phys. Chem. Chem. Phys. 2000; 2:2187–2193.
40. Wachters A. Gaussian basis set for molecular wave functions containing third-row atoms. J. Chem. Phys. 1970; 52:1033–1036.
41. Hay PJ. Gaussian basis sets for molecular calculations. The representation of 3*d* orbitals in transition-metal atoms. J. Chem. Phys. 1977; 66:4377–4384.
42. McLean AD, Chandler GS. Contracted Gaussian basis sets for molecular calculations. I. Second row atoms, *Z*=11–18. J. Chem. Phys. 1980; 72:5639–5648.
43. Krishnan R, Binkley JS, Seeger R, Pople JA. Self-consistent molecular orbital methods. XX. A basis set for correlated wave functions. J. Chem. Phys. 1980; 72:650–654.
44. Mennucci B, Tomasi J. Continuum solvation models: a new approach to the problem of solute's charge distribution and cavity boundaries. J. Chem. Phys. 1997; 106:5151–5158.
45. Mennucci B, Cancès E, Tomasi J. Evaluation of solvent effects in isotropic and anisotropic dielectrics and in ionic solutions with a unified integral equation method: theoretical bases, computational implementation, and numerical applications. J. Phys. Chem. B. 1997; 101:10506–10517.
46. Cammi R, Mennucci B, Tomasi J. Second-order Møller–Plesset analytical ferivatives for the polarizable continuum model using the relaxed density approach. J. Phys. Chem. A. 1999; 103:9100–9108.
47. Cammi R, Mennucci B, Tomasi J. Fast evaluation of geometries and properties of excited molecules in solution: a Tamm-Dancoff model with application to 4-dimethylamino-enzonitrile. J. Phys. Chem. A. 2000; 104:5631–5637.
48. Leu BM, et al. Quantitative vibrational dynamics of iron in nitrosyl porphyrins. J. Am. Chem. Soc. 2004; 126:4211–4227. [PubMed: 15053610]
49. Tenderholt A. gennrvs, Pymol script. 2009 available at http://www.stanford.edu/group/solomon/gennrvs/gennrvs.py.txt.
50. Srnec M, et al. Structural and Spectroscopic properties of the peroxodiferric intermediate of *Ricinus communis* soluble Δ^9 desaturase. Inorg. Chem. 2012; 51:2806–2820. [PubMed: 22332845]
51. Becke AD. Density-functional thermochemistry. III. The role of exact exchange. J. Chem. Phys. 1993; 98:5648.
52. Lee C, Yang W, Parr R. Development of the Colle-Salvetti correlation-energy formula into a functional of the electron density. Phys. Rev. B. 1988; 37:785–789.
53. Miehlich B, Savin A, Stoll H, Preuss H. Results obtained with the correlation energy density functionals of Becke and Lee, Yang and Parr. Chem. Phys Lett. 1989; 157:200–260.
54. Grimme S. Accurate description of van der Waals complexes by density functional theory including empirical corrections. J. Comput. Chem. 2004; 25:1463–1473. [PubMed: 15224390]
55. Grimme S. Semiempirical GGA-type density functional constructed with a long-range dispersion correction. J. Comput. Chem. 2006; 27:1787–1799. [PubMed: 16955487]

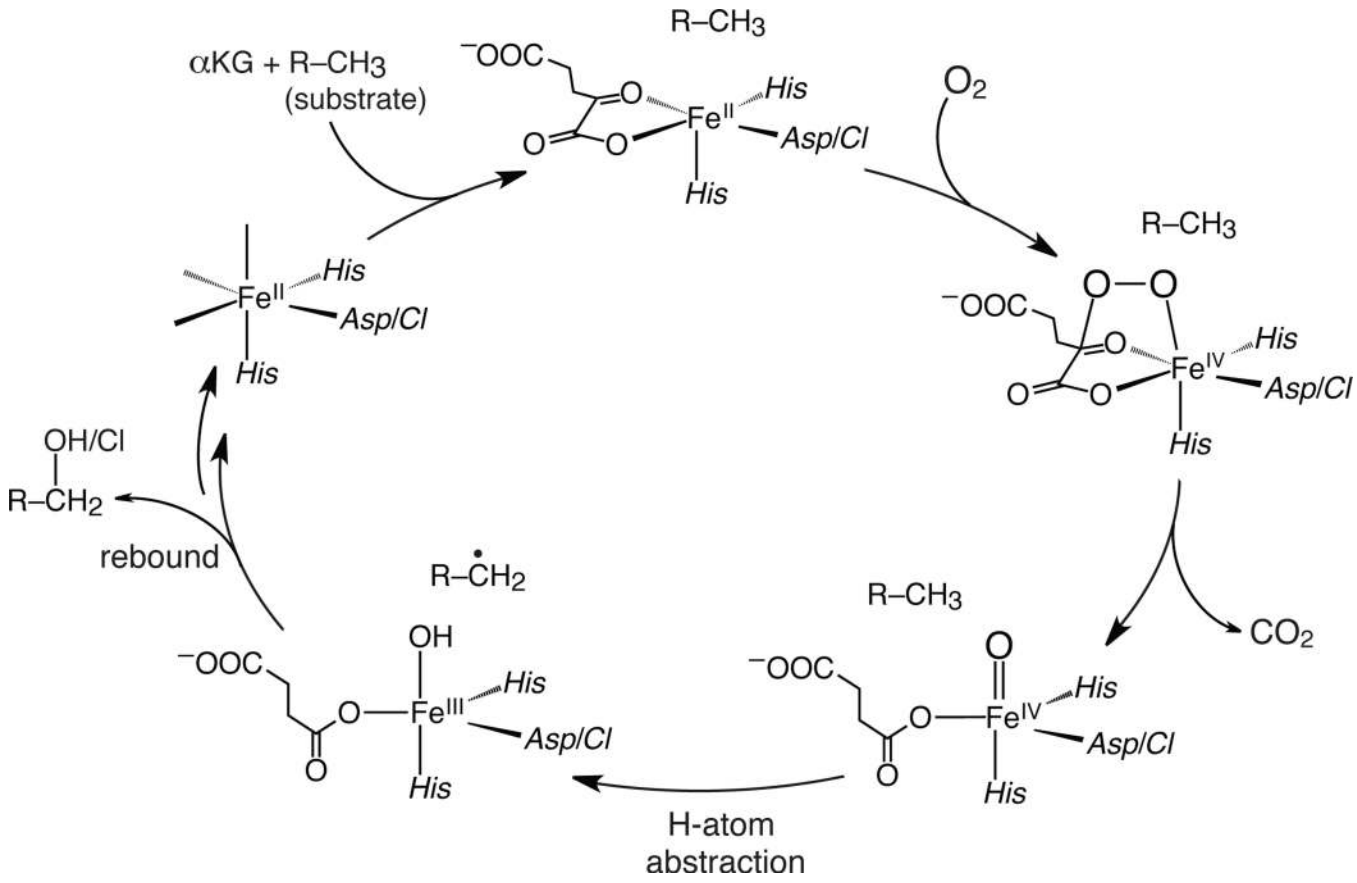

Figure 1.

Catalytic cycle of αKG-dependent NHFe enzymes. αKG and substrate binding induces a 6-coordinate → 5-coordinate conversion (*top*), providing a site for O_2 to bind and form an Fe^{IV}—peroxo species that nucleophilically attacks αKG, producing a peroxo-bridged Fe^{IV} species (*right*).[24] Decarboxylation of αKG leads to the reactive Fe^{IV}=O intermediate (*bottom right*).

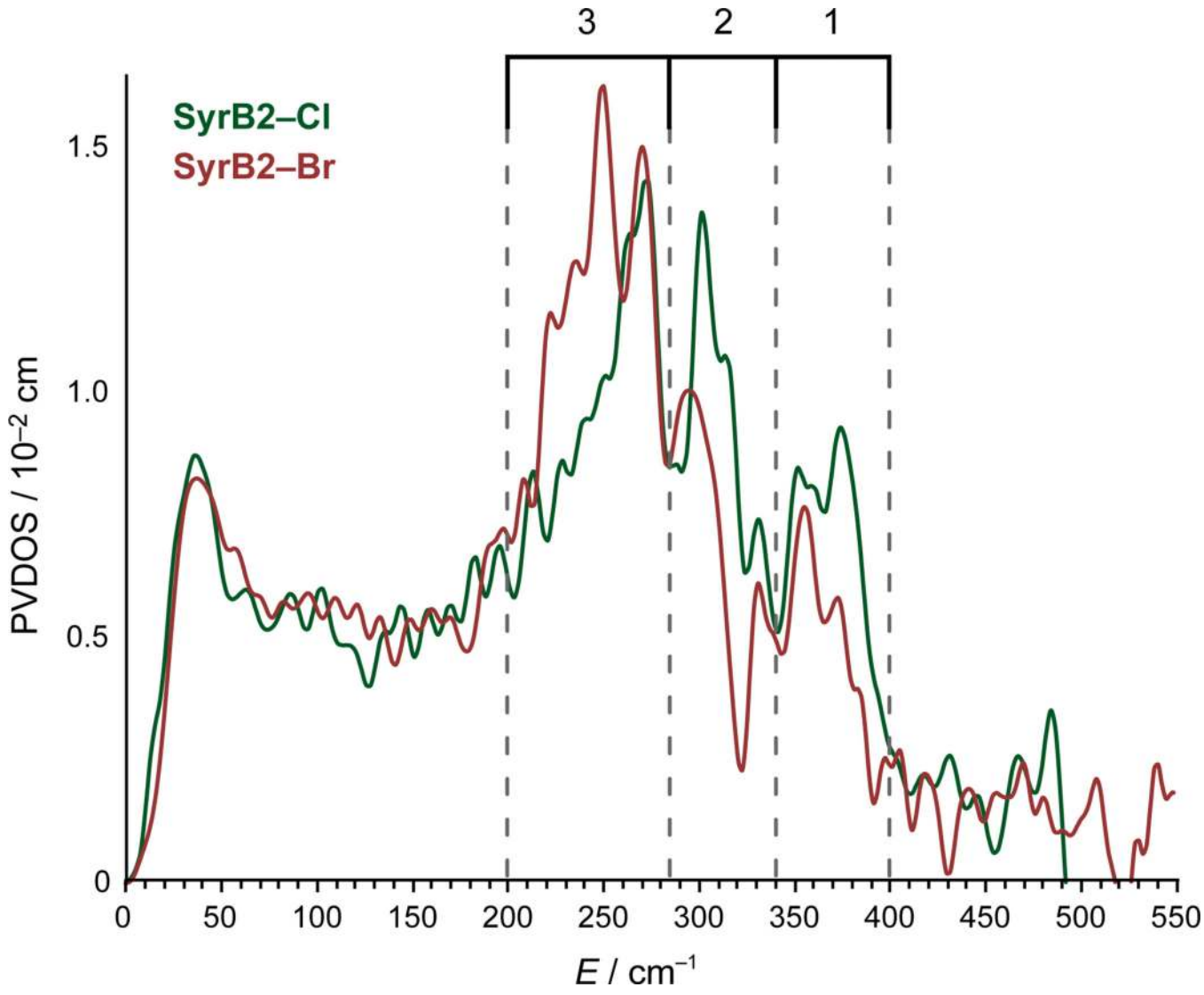

Figure 2.

NRVS PVDOS spectra of SyrB2–Cl and SyrB2–Br, with regions containing intense features indicated in brackets.

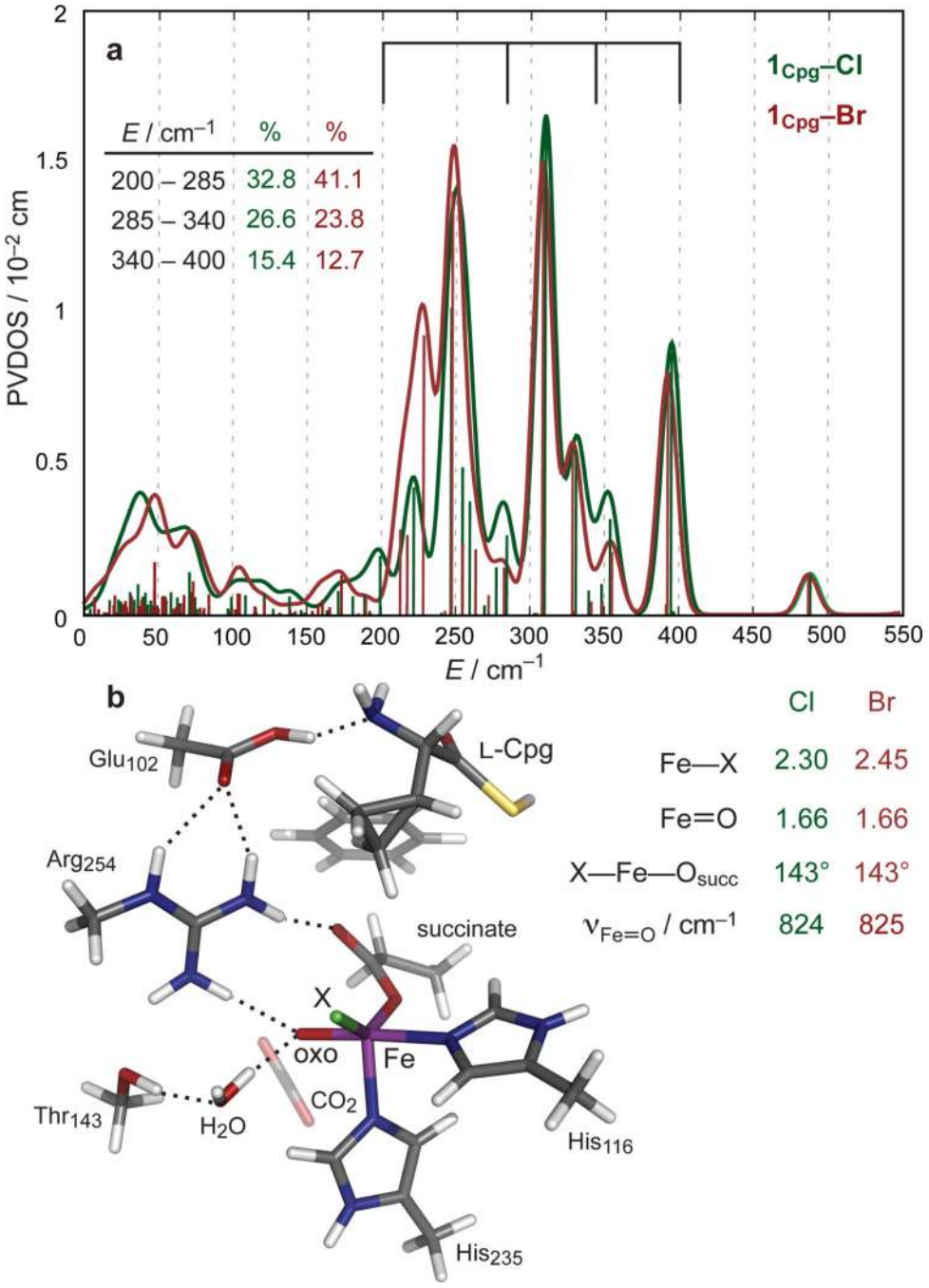

Figure 3.

a, DFT-predicted PVDOS NRVS spectra of 5C TBP structural candidate $\mathbf{1_{Cpg}–X}$ for Fe^{IV}=O intermediate of SyrB2. Vertical bars represent relative calculated mode-composition factors of vibrational modes, and brackets correspond to energy regions from Fig. 2. (*Inset*) Peak intensity contributions (from three bracketed regions) to overall PVDOS envelope. **b,** Structure of $\mathbf{1_{Cpg}–X}$ (*left*), along with geometric parameters and Fe—oxo stretching frequencies (*right*).

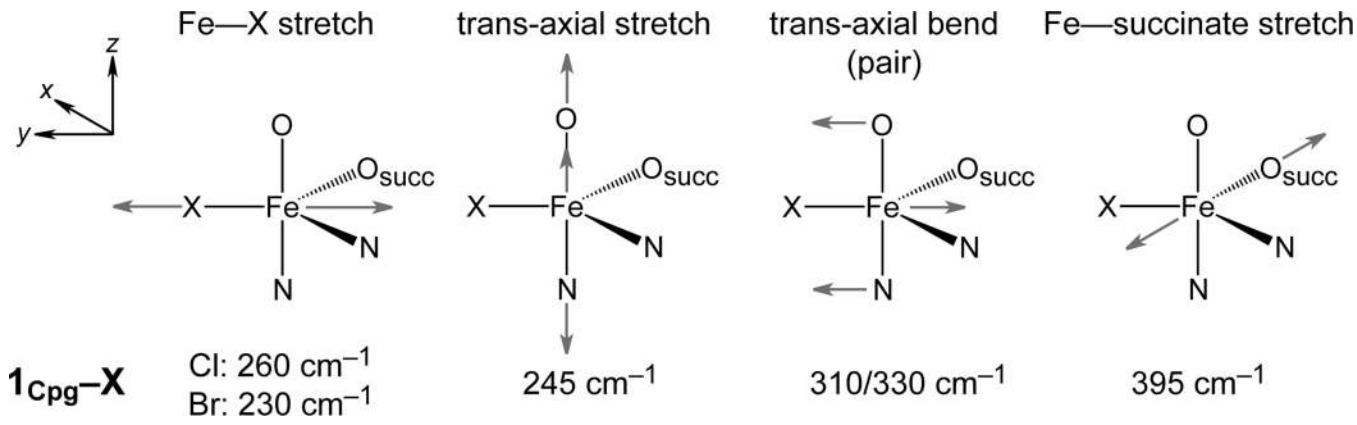

Figure 4.

DFT-predicted normal modes of 5C TBP Fe^{IV}=O structures $\mathbf{1_{Cpg}–X}$, with corresponding frequencies. The Fe—oxo vector defines the *z*-axis.

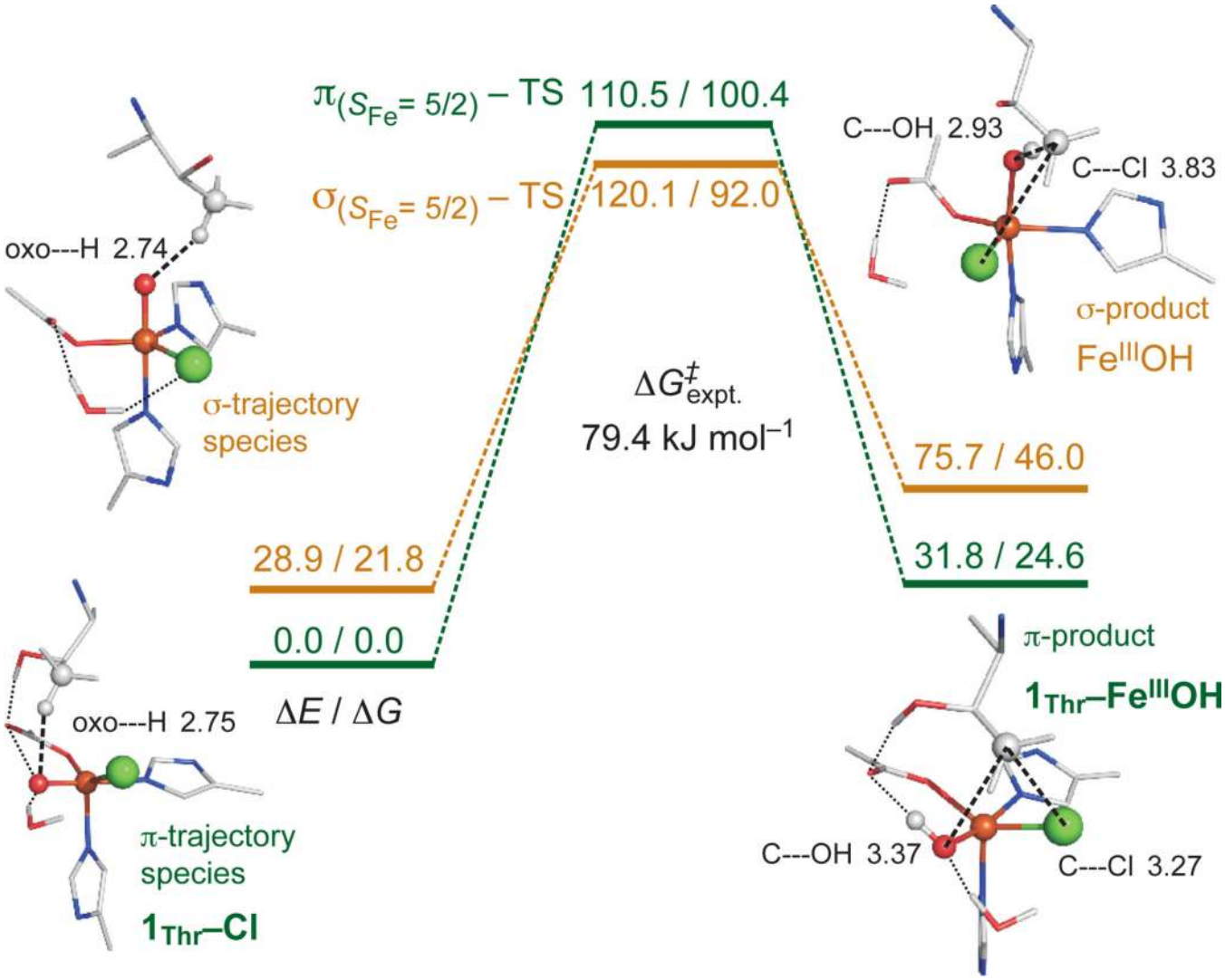

Figure 5.

H-atom abstraction reaction coordinates for π-trajectory (**1_{Thr}–Cl**, green) and σ-trajectory (orange), with energies (Δ*E*/Δ*G*) given in kJ mol^{-1}. Structures of $Fe^{III}_{(S=5/2)}$—OH products displayed on right (with distances in Å), showing **1_{Thr}–Fe^{III}OH** (with hydrogen-bonding interactions indicated) set up for chlorination and σ-product set up for hydroxylation. For additional structural details, see Supplementary Fig. 11.